NANO LETTERS

Letter

pubs.acs.org/NanoLett

# Room Temperature O-band DFB Laser Array Directly Grown on (001) Silicon

Bin Tian,[†,‡] Zhechao Wang,[*,†,‡,§] Marianna Pantouvaki,[§] Philippe Absil,[§] Joris Van Campenhout,[§] Clement Merckling,[*,§] and Dries Van Thourhout[†,‡]

[†]Department of Information Technology (INTEC), Ghent University, iGent, Technologiepark-Zwijnaarde 15, B-9052 Gent, Belgium

[‡]Center for Nano- and Biophotonics (NB-Photonics), Ghent University, iGent, Technologiepark-Zwijnaarde 15, B-9052 Gent, Belgium

[§]IMEC, Kapeldreef 75, 3001 Heverlee, Belgium

**ABSTRACT:** Several approaches for growing III−V lasers on silicon were recently demonstrated. Most are not compatible with further integration, however, and rely on thick buffer layers and require special substrates. Recently, we demonstrated a novel approach for growing high quality InP without buffer on standard 001-silicon substrates using a selective growth process compatible with integration. Here we show high quality InGaAs layers can be grown on these InP-templates. High-resolution TEM analysis shows these layers are free of optically active defects. Contrary to InP, the InGaAs material exhibits strong photoluminescence for wavelengths relevant for integration with silicon photonics integrated circuits. Distributed feedback lasers were defined by etching a first order grating in the top surface of the device. Clear laser operation at a single wavelength with strong suppression of side modes was demonstrated. Compared to the previously demonstrated InP lasers 65% threshold reduction is observed. Demonstration of laser arrays with linearly increasing wavelength prove the control of the process and the high quality of the material. This is an important result toward realizing fully integrated photonic ICs on silicon substrates.

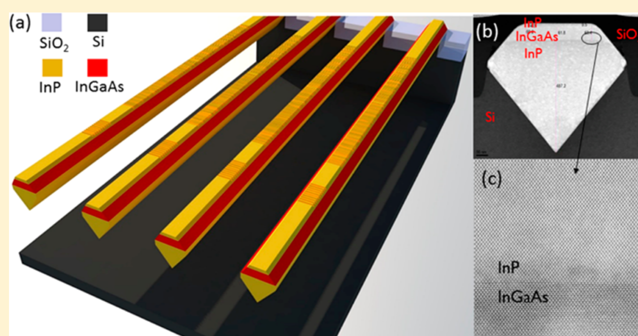


**KEYWORDS:** *DFB laser array, semiconductor laser, metal organic chemical vapor phase epitaxy, heteroepitaxy, silicon photonics*

Since the initial work on silicon photonics,[1−4] the lack of on-chip optical amplifiers and lasers has been the fundamental obstacle limiting the application scope of this technology platform. A number of solutions exploring engineered group IV materials and their alloys have been proposed,[5,6] but high-efficiency and room temperature operation could not yet be demonstrated. Solutions integrating III−V materials using flip-chip and bonding technologies are now commercially available for intradata center optical interconnects.[7−9] However, in that case one only partially benefits from the economies of scale offered by the well-established manufacturing infrastructure of the electronics industry, which is the main driver fueling the massive investments in silicon photonics. Therefore, there is a strong drive to develop methods allowing the monolithic integration of III−Vs on silicon using wafer-scale epitaxial growth technologies. However, given the fact that III−V materials and silicon are very different in terms of lattice constant, thermal expansion coefficient, and surface polarity, the as-grown samples are typically highly defective, being full of misfit and threading dislocations, twins, stacking faults, and antiphase boundaries, detrimental for photonic devices.[10] Substantial progress has been made in the past few years on heteroepitaxy of III−Vs on silicon.[11−13] Recently a novel localized growth technique, initially developed by the electronics industry for next generation CMOS devices, has shown to deliver low-defect-density growth of III−V waveguides directly on standard (001)-oriented silicon substrate with most of the defects confined into a 20 nm thick buffer layer.[14−16] Leveraging this technique for photonics, we demonstrated the wafer-scale monolithic integration of InP distributed feedback (DFB) laser arrays directly on silicon.[17]

In this work, we take another step forward and show that these InP-on-Si structures can serve as a virtual III−V substrate for subsequent growth of high quality III−V epitaxial stacks. By growing an InP/InGaAs/InP heterostructure on the aforementioned InP virtual substrate, we demonstrate a room-temperature optically pumped DFB laser emitting within the 1300 nm wavelength range, where silicon is transparent and therefore is more favorable for silicon photonics based applications. The use of a well-understood in-plane laser configuration (distributed feedback laser cavity) and the top down processing flow made it straightforward to demonstrate

**Received:** November 9, 2016
**Revised:** December 18, 2016
**Published:** December 20, 2016

ACS Publications © 2016 American Chemical Society



DOI: 10.1021/acs.nanolett.6b04690
*Nano Lett.* 2017, 17, 559−564

an array of lasers emitting within the O-band with good control over the central wavelength.

Figure 1a schematically depicts the layout of the finalized InGaAs/InP/Si distributed feedback (DFB) laser array. The

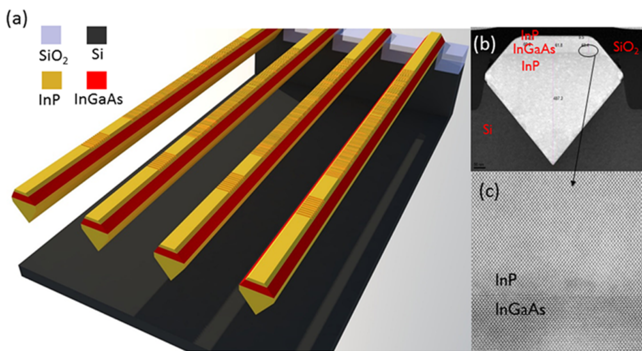


**Figure 1.** (a) Schematic plot of the monolithically integrated InGaAs/InP DFB lasers on silicon. The silicon pedestal (and the silicon oxide hard mask) under the near end has been removed for a better view of the III−V waveguide. (b) STEM image of a typical cross-section of the grown InGaAs/InP/Si waveguide. (c) A zoom-in STEM image of the InGaAs/InP interface.

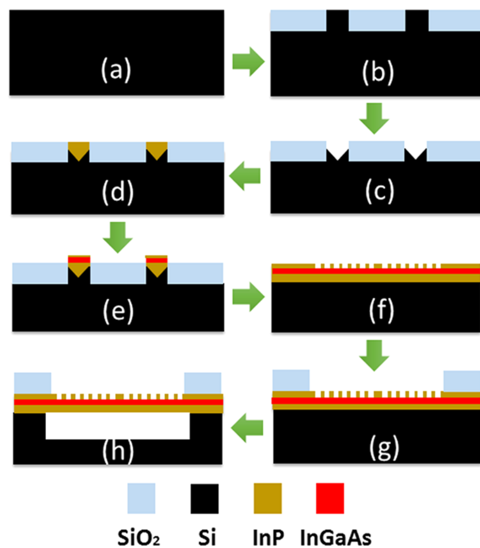


**Figure 2.** Integration process starts from (a) a standard (001) silicon substrate. (b) Trenches are defined by an STI process. (c) V-shaped grooves are formed by anisotropic wet etching. (d) InP is selectively grown in V-shaped trenches, followed by chemical mechanical polishing. (e) Regrowth of the InGaAs/InP heterostructure on the InP-on-Si virtual substrate. (f) Gratings are defined by electron beam lithography and dry etching. (g) Silicon oxide hard mask is defined by optical lithography and dry etching. (h) The silicon substrate is undercut by reactive ion etching.

fabrication process is outlined in Figure 2. Starting from a standard (001)Si substrate, 500 nm wide silicon ridges embedded in a $SiO_2$ buffer are patterned by a shallow trench isolation (STI) process.[18] The silicon material inside the trenches is then anisotropically etched away using tetramethylammonium hydroxide (TMAH) to expose the ⟨111⟩ Si facets in the bottom of the trenches.[14,18] Next, InP is selectively grown inside the trenches by metal organic chemical vapor phase epitaxy (MOPVE)[19] and the surface is planarized using an optimized chemical mechanical polishing (CMP) process.[20] An $In_xGa_{1-x}As$ ternary compound layer and an InP passivation layer are grown subsequently on top of the planarized InP-on-Si virtual substrate. Bragg gratings are then defined on the top surface of the InP/$In_xGa_{1-x}As$/InP waveguide by electron-beam lithography (EBL) and inductively coupled plasma (ICP) dry etching, with a quarter wave phase shift section inserted in the middle to ensure stable single wavelength operation (Figure 2f). To facilitate vertical light extraction, a short second order grating is defined in front of each DFB laser. The expected emission wavelength of 1300 nm is well below the silicon band-edge and therefore no absorption in the substrate is expected. However, the high refractive index of the silicon material can cause large leakage loss that inhibits lasing. Therefore, a soft dry etch process is developed to partially remove the silicon underneath the laser cavity (Figure 2 g,h). The suspended laser cavity (100 $\mu$m in length) is supported by silicon pedestals at both edges. Two extra passive waveguides (200 $\mu$m in length with no grating defined on top) are inserted between the laser cavity and the pedestals to minimize optical reflections. In order to avoid using a suspended cavity and therefore to obtain better mechanical stability and improved thermal dissipation, the ultimate solution would be to grow the III−V heterostructures on top of a silicon-on-insulator wafer.

As first demonstrated in our previous work,[17] despite the huge mismatch in intrinsic material properties between Si and InP ($\varepsilon_{InP/Si}$ = 8.06%), using the selective area epitaxial process outlined above, high quality InP can be grown directly on silicon with most of the defects confined to a very thin (~20 nm) layer at the InP/Si interface. In Figure 1b, a high-angle annular dark-field (HAADF) scanning transmission electron microscopy (STEM) image of the cross section parallel orthogonal to the trench direction of a typical InP/$In_xGa_{1-x}As$/InP/Si waveguide is shown, demonstrating the high material quality of the grown III−V heterostructure. Although a few twins or stacking faults, which are initiated during the initial InP islands coalescence process step,[19] cannot be fully eliminated, the epitaxial layer stack is free of threading locations in all TEM specimens. Moreover, by introducing the V-shaped grooves, the formation of antiphase boundaries is inhibited[14] as confirmed by the TEM cross sections in both perpendicular and parallel trench orientations. Figure 1c is a zoom-in HAADF-STEM image at the $In_xGa_{1-x}As$/InP-on-Si interfacial region. For a typical waveguide, the thickness of the InP-buffer is around 500 nm, the thickness of the $In_xGa_{1-x}As$ layer is about 60 nm, and the InP passivation layer is around 20 nm thick. One can find a very abrupt transition from the InP to the $In_xGa_{1-x}As$ layer without evidence of misfits or threading dislocations. As described in Figure 2d,e, a chemical mechanical polishing (CMP) process was employed to obtain a flat (001)-oriented InP top surface prior to the growth of the $In_xGa_{1-x}As$ layer. Optimization of the CMP process and the in situ cleaning step right before the InGaAs growth proved to be critical in obtaining a high quality heterostructure interface.

In Figure 3, the elemental mapping by energy-dispersive X-ray spectroscopy (EDS) is presented, confirming the sharp transitions at all InP/Si and InP/$In_xGa_{1-x}As$/InP interfaces. From the EDS measurement, the indium content of the $In_xGa_{1-x}As$ layer is found to be around 35%, and therefore the $In_{0.35}Ga_{0.65}As$ layer on top of the fully relaxed InP buffer is tensile strained. In Figure 3(f), a TEM image of the InP/$In_xGa_{1-x}As$/InP/Si waveguide along the longitudinal direction


DOI: 10.1021/acs.nanolett.6b04690
Nano Lett. 2017, 17, 559−564

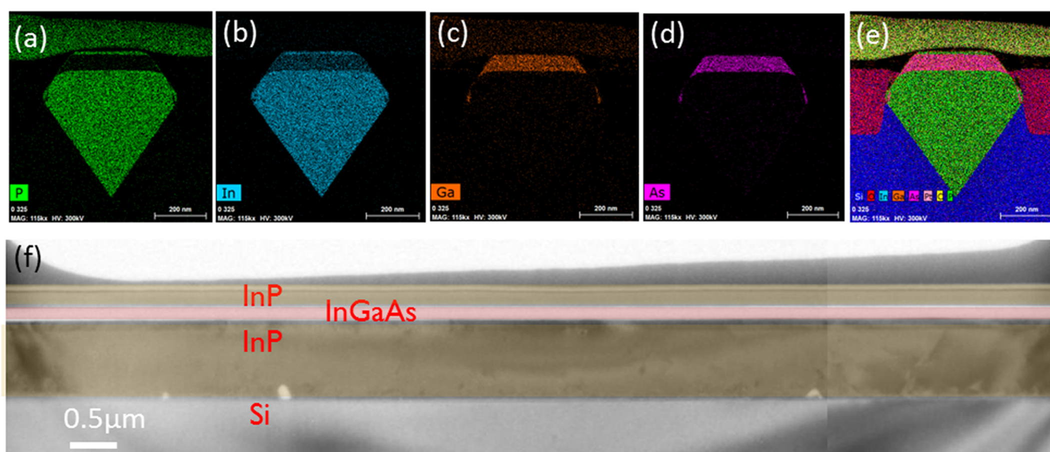


**Figure 3.** Elemental mapping of the grown InGaAs/inP/Si heterostructure by EDS, (a) phosphorus, (b) indium, (c) gallium, (d) arsenide, (e) and combined view of all elements above. (f) Large-scale TEM picture along the waveguide.

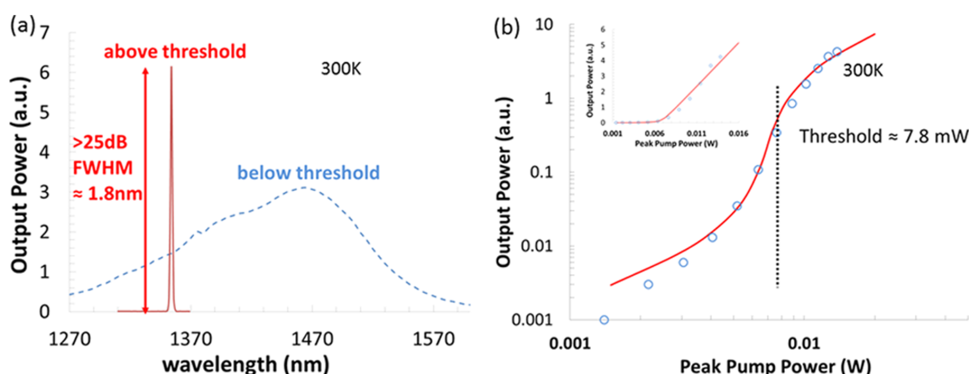


**Figure 4.** (a) Room-temperature emission spectrum below (blue dashed) and above (red solid line) threshold. (b) L−L curve of the DFB laser on a double logarithmic scale. Circles are the measured data, the solid curve is a rate equation fit. Inset: plot of the L−L curve on a linear scale.

is presented, which demonstrates the high quality of the hetero interfaces seen over a much longer section. Similar to the conclusion obtained above, the grown layer stack is free of threading dislocations, although a few planar defects are still visible along the trench orientation. More detailed TEM characterizations of similar heterostructures can be found elsewhere.[21] Because of the nature of the confined growth, we estimate the defect density to be around 0.2#/$\mu$m. While these planar defects may not be active in optically pumped devices,[15] they may play a role during the aging of electrically pumped lasers to which dark line defects have been observed to be correlated. In that case, active regions based on quantum dots or quantum dashes can be employed in the future as they have been proven to be robust against such defects.[11]

The devices were characterized on a microphotoluminescence ($\mu$-PL) setup, consisting of a Nd:YAG nanosecond pulsed laser (7 ns pulse width, 938 Hz repetition rate, 1064 nm wavelength) or a Nd:YAG continuous wave (CW) laser (1064 nm wavelength) as the pump source, a X50, 0.65 numerical aperture objective, a 0.25 m monochromator, and a thermoelectric-cooled InGaAs detector. A lock-in amplifier is used to improve the signal-to-noise ratio. Spatial filters are used to limit the pumping area to a rectangular area 5 $\mu$m in width and 200 $\mu$m in length, covering only a single device, although parts of the passive waveguides at two sides of the device are also pumped. The characterized device exhibits a first order grating of 359 nm period and 50% duty cycle. The etching depth of the grating is 20 nm such that only the InP cap layer is etched away without damaging the $In_{0.35}Ga_{0.65}As$ active layer.

Figure 4a (dashed curve) presents the below threshold PL spectrum measured using the CW pump source. A broad photoluminescence spectrum centered at 1460 nm is obtained (fwhm 150 nm, 96 meV). As discussed above, from the elemental mapping the indium content of the InGaAs layer is derived to be about 35%. Ignoring strain, the bandgap energy of an $In_xGa_{1-x}As$ layer can be calculated as[22]

$$E_g = 0.324 + 0.7x + 0.4x^2 \text{ (eV)} \quad (1)$$

in which $x$ is the indium content, that is, 0.35 in our case. The unstrained bandgap is therefore calculated to be 0.948ev (1300 nm). Assuming a uniformily two-dimensionally (2D) strained layer on an InP substrate, an InGaAs layer with 35% indium content exhibits a 1.27% tensile strain due to the lattice mismatch with the InP substrate. This tensile strain lifts the degeneracy of the heavy hole and light hole bands, resulting in the following transition energies (taking into account spin−orbit split-off band coupling[23])

$$E_{C-HH} = 0.8909 \text{ eV } (1.39\ \mu\text{m}) \quad (2)$$

$$E_{C-LH(SO)} = 0.7954 \text{ eV } (1.56\ \mu\text{m}) \quad (3)$$

Different from a uniformly 2D strained layer, the presented submicron scaled III−V waveguide is suspended in air, and therefore the free boundaries might allow the strain of the


DOI: 10.1021/acs.nanolett.6b04690
Nano Lett. 2017, 17, 559−564

heterostructure to relax due to deformation. Figure 5 plots the calculated transition energies as a function of the strain relaxation in the transversal cross-section of the device due to deformation (1, fully 2D-strained; 0, fully relaxed in transversal direction, fully strained in longitudinal direction). As no dislocations (e.g., Figure 1c, Figure 2.f) are found at the InP/InGaAs heterointerface it is assumed there is no strain relaxation in the longitudinal direction. For comparison, the measured PL spectrum of the InGaAs layer is also shown in Figure 5. We can conclude that the below threshold spectrum most likely originates from both HH and LH transitions as the two peaks in the spectrum approximately match the transition energies predicted by the calculations.

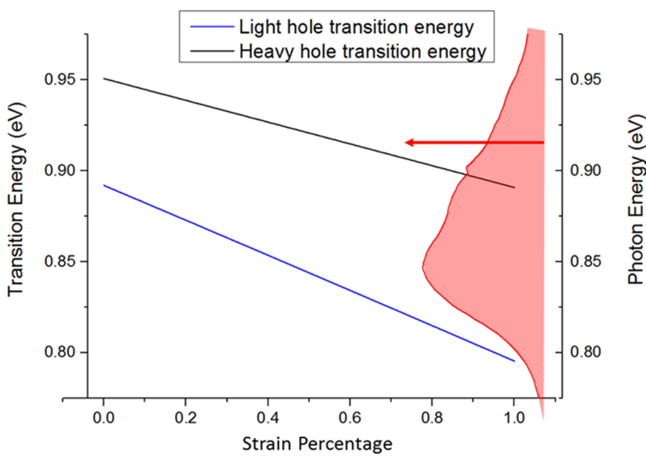


**Figure 5.** Transition energy changes as a function of the strain relaxation in transversal direction along the interface between InGaAs and InP layers (1, fully 2D-strained, 0, fully relaxed in transversal direction). The solid black and blue lines are the transition energy from the heavy hole and light hole bands, respectively. The red area shows the PL spectrum under CW pumping and the arrow indicates the photon energy at which lasing operation is achieved.

As shown in Figure 4a, under pulsed pumping a resonance peak appears around 1354 nm and a maximal side mode suppression ratio better than 25 dB is obtained. The full width half-maximum (fwhm) of the peak is 1.8 nm, mainly limited by the carrier density modulation during the pulsed pumping.[17,24] Figure 3b plots the output power as a function of the input peak power (Light in−light out (L−L) curve) both on a linear and a logarithmic scale. The clear change in the slope of the curves is a strong indication of laser operation. Taking into account the system loss of the PL setup and assuming a constant power level within the 7 ns pump pulse, the laser threshold is derived to be 7.8 ± 1.3 mw.

To understand the nature of the lasing optical mode in this relatively large waveguide, finite-difference time-domain (FDTD) simulations were carried out. Considering that the device is lasing at an energy level above the light hole to conduction band transition energy (see the red arrow in Figure 5) and the applicable selection rules in the bulk InGaAs layer favor TE-polarization for the conduction band to heavy hole band transition, quasi-TE modes were analyzed first.

The simulation results are presented in Figure 6, which shows the calculated reflection spectra of the fabricated grating plotted together with the corresponding optical mode profiles. While the reflection peak associated with the fundamental TE mode is located far away from the lasing wavelength, the TE11 mode exhibits a high reflection around the measured lasing wavelength and a high confinement in the active area. Therefore, one can assume the TE11 mode to be the lasing mode. The deviation between the measured lasing wavelength and the calculated stopband of the TE11 mode is believed to originate from uncertainty in the refractive index of the nonuniformly strained InGaAs layer (the refractive index of an unstrained $In_{35}Ga_{65}As$ layer is used for the simulation with the material dispersion estimated from the Sellmeier equation). Also quasi-TM modes were analyzed but no modes exhibiting substantial overlap with the InGaAs layer were found, further confirming the lasing mode most probably has a quasi-TE character.

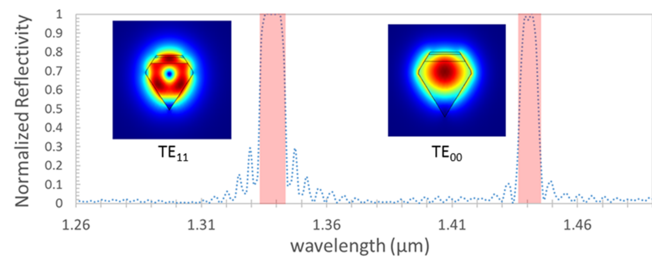


**Figure 6.** Reflection spectra and the corresponding optical mode profiles of the grating with a 360 nm period and a 50% duty cycle. (Left insert) TE11 mode, effective index = 1.78, confinement factor = 10.7%. (Right insert) fundamental TE mode, effective index = 2.51, confinement factor = 13.1%.

Comparing the threshold pump power of the demonstrated InGaAs/InP heterostructure laser with the InP DFB laser presented earlier,[17] we find a substantial reduction of about 65%. This improvement mainly stems from the following three factors: (1) Using a pump source with a wavelength close to the bandgap of the gain material, less input power is wasted through heat dissipation. (2) Compared with the pure InP DFB laser, the volume of active material that needs to be inverted is substantial smaller. (3) Compared with the pure InP DFB laser, in which the generated carriers are distributed evenly across the whole waveguide, the InP/InGaAs/InP heterostructure employed in the current case confines the carriers largely to the gain region and therefore prevents nonradiative recombination at the defective waveguide sidewalls.

Because of its small fiber loss and low chromatic dispersion, the so-called O band of 1260−1360 nm is widely used in telecommunications. A wavelength division multiplexing (WDM) system that covers most of this band could dramatically increase the bandwidth of next generation optical interconnects. Given the use of a well-understood in-plane laser cavity configuration, and the top-down processing flow illustrated in Figure 2, it is straightforward to implement single mode laser arrays with precise control over their emission wavelength. To demonstrate the potential for scaling of the presented integration platform, an array of 10 DFB lasers with the grating period being varied from 335 to 362 nm was fabricated. The duty cycle and etching depth were kept at 50% and 20 nm, respectively.

The laser array was characterized using the same methodology as outlined above for the stand alone device, isolating the individual lasers for each measurement. The measured optical spectra of all ten lasers are shown in Figure 7a on a double logarithmic scale. The peak wavelength of the lasers shifts uniformly as the grating period changes and the output power of the laser array is relatively uniform. As shown in Figure 7b,


DOI: 10.1021/acs.nanolett.6b04690
Nano Lett. 2017, 17, 559−564

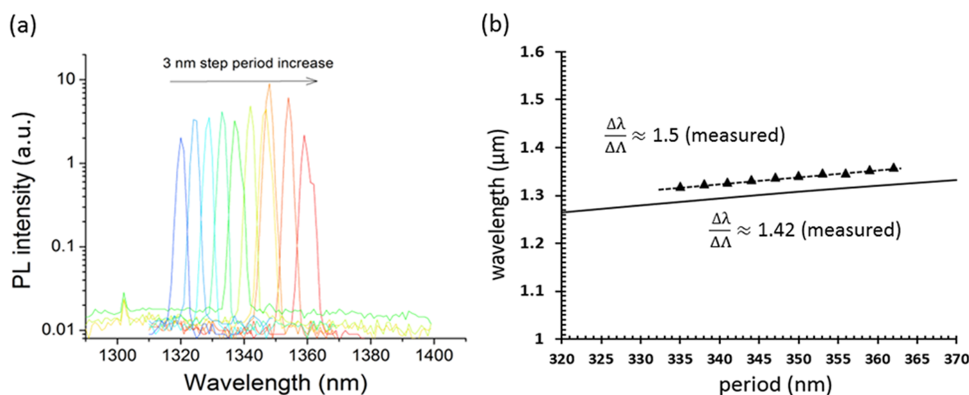


**Figure 7.** (a) Measured lasing spectra of the DFB laser array, demonstrating the capability to control the laser wavelength through grating design. (b) The laser wavelengths measured from the DFB laser array (black triangle) and the simulated lasing wavelength (black solid line).

the slope of the laser wavelength versus grating period is extracted to be 1.5, which is very close to the simulated value (1.42). A 2.5% mismatch of the lasing wavelength is found between the measurements and simulations. This small discrepancy can be attributed to the uncertainty of the refractive index of the InGaAs as has already discussed above.

In conclusion, we demonstrated an in-plain monolithic integrated O-band DFB laser array on silicon. The lasing wavelength can be well controlled, and compared with the previously presented pure InP laser array, the O-band source is more favorable for the optical interconnects industry because of the transparency of the emitting wavelength in the silicon material and the better control of the injected carriers that results in lower lasing threshold. More importantly, this work proves that the InP/Si platform can serve as a virtual lattice matched substrate for growing more complex epi stacks on top, which makes it a universal platform for various applications.

Moving forward, the next step will be a fully functional, low threshold electrically pumped laser. The current suspended laser is not a good candidate to achieve this goal because it does not allow for current injection and inhibits efficient heat dissipation. Growing III−V on SOI substrates can overcome these issues by separating the optical mode from the substrate, improving heat dissipation, and facilitating electrical injection.

## ■ AUTHOR INFORMATION

### Corresponding Authors

*E-mail: zhechao.wang@intec.UGent.be. Phone: +32-9-261 4817. Fax: +32-9-264 3593.
*E-mail: Clement.Merckling@imec.be. Phone: +32 16 28 82 75. Fax: +32 16 22 94 00.

### ORCID

Zhechao Wang: 0000-0003-4767-6254

### Author Contributions

The manuscript was written through contributions of all authors. All authors have given approval to the final version of the manuscript.

### Notes

The authors declare no competing financial interest.

## ■ ACKNOWLEDGMENTS

This work was supported through the EU ERC starting grant ULPPIC, imec's industry-affiliation program on optical I/O, and the Belgian Science Policy Office (IAP P7/35−photonics@ be).

## ■ REFERENCES

(1) Soref, R. *IEEE J. Sel. Top. Quantum Electron.* **2006**, *12* (6), 1678−1687.
(2) Miller, D. A. B. *Proc. IEEE* **2009**, *97* (7), 1166−1185.
(3) Gunn, C. *Ieee Micro* **2006**, *26* (2), 58−66.
(4) Ohashi, K.; Nishi, K.; Shimizu, T.; Nakada, M.; Fujikata, J.; Ushida, J.; Torii, S.; Nose, K.; Mizuno, M.; Yukawa, H.; Kinoshita, M.; Suzuki, N.; Gomyo, A.; Ishi, T.; Okamoto, D.; Furue, K.; Ueno, T.; Tsuchizawa, T.; Watanabe, T.; Yamada, K.; Itabashi, S.; Akedo, J. *Proc. IEEE* **2009**, *97* (7), 1186−1198.
(5) Liu, J. F.; Sun, X. C.; Camacho-Aguilera, R.; Kimerling, L. C.; Michel, J. *Opt. Lett.* **2010**, *35* (5), 679−681.
(6) Wirths, S.; Geiger, R.; von den Driesch, N.; Mussler, G.; Stoica, T.; Mantl, S.; Ikonic, Z.; Luysberg, M.; Chiussi, S.; Hartmann, J. M.; Sigg, H.; Faist, J.; Buca, D.; Grützmacher, D. *Nat. Photonics* **2015**, *9* (2), 88−92.
(7) Fang, A. W.; Park, H.; Cohen, O.; Jones, R.; Paniccia, M. J.; Bowers, J. E. *Opt. Express* **2006**, *14* (20), 9203−10.
(8) Van Campenhout, J.; Rojo Romeo, P.; Regreny, P.; Seassal, C.; Van Thourhout, D.; Verstuyft, S.; Di Cioccio, L.; Fedeli, J. M.; Lagahe, C.; Baets, R. *Opt. Express* **2007**, *15* (11), 6744−9.
(9) Liu, L.; Kumar, R.; Huybrechts, K.; Spuesens, T.; Roelkens, G.; Geluk, E.-J.; de Vries, T.; Regreny, P.; Van Thourhout, D.; Baets, R.; Morthier, G. *Nat. Photonics* **2010**, *4* (3), 182−187.
(10) Ayers, J. E. *Heteroepitaxy of Semiconductors - Theory, Growth, and Characterization*; CRC Press: New York, 2007.
(11) Chen, S.; Li, W.; Wu, J.; Jiang, Q.; Tang, M.; Shutts, S.; Elliott, S. N.; Sobiesierski, A.; Seeds, A. J.; Ross, I.; Smowton, P. M.; Liu, H. *Nat. Photonics* **2016**, *10* (5), 307−311.
(12) Wan, Y.; Li, Q.; Liu, A. Y.; Gossard, A. C.; Bowers, J. E.; Hu, E. L.; Lau, K. M. *Opt. Lett.* **2016**, *41* (7), 1664−1667.
(13) Tournié, E.; Cerutti, L.; Rodriguez, J.-B.; Liu, H.; Wu, J.; Chen, S. *MRS Bull.* **2016**, *41* (3), 218−223.
(14) Paladugu, M.; Merckling, C.; Loo, R.; Richard, O.; Bender, H.; Dekoster, J.; Vandervorst, W.; Caymax, M.; Heyns, M. *Cryst. Growth Des.* **2012**, *12* (10), 4696−4702.
(15) Wang, Z.; Tian, B.; Paladugu, M.; Pantouvaki, M.; Le Thomas, N.; Merckling, C.; Guo, W.; Dekoster, J.; Van Campenhout, J.; Absil, P.; Van Thourhout, D. *Nano Lett.* **2013**, *13* (11), 5063−9.
(16) Guo, W.; Date, L.; Pena, V.; Bao, X.; Merckling, C.; Waldron, N.; Collaert, N.; Caymax, M.; Sanchez, E.; Vancoille, E.; Barla, K.; Thean, A.; Eyben, P.; Vandervorst, W. *Appl. Phys. Lett.* **2014**, *105* (6), 062101.
(17) Wang, Z.; Tian, B.; Pantouvaki, M.; Guo, W.; Absil, P.; Van Campenhout, J.; Merckling, C.; Van Thourhout, D. *Nat. Photonics* **2015**, *9* (12), 837−842.
(18) Wang, G.; Leys, M. R.; Nguyen, N. D.; Loo, R.; Brammertz, G.; Richard, O.; Bender, H.; Dekoster, J.; Meuris, M.; Heyns, M. M.; Caymax, M. *J. Electrochem. Soc.* **2010**, *157* (11), H1023−H1028.


DOI: 10.1021/acs.nanolett.6b04690
*Nano Lett.* 2017, 17, 559−564

(19) Merckling, C.; Waldron, N.; Jiang, S.; Guo, W.; Collaert, N.; Caymax, M.; Vancoille, E.; Barla, K.; Thean, A.; Heyns, M.; Vandervorst, W. *J. Appl. Phys.* **2014**, *115* (2), 023710.
(20) Waldron, N.; Merckling, C.; Guo, W.; Ong, P.; Teugels, L.; Ansar, S.; Tsvetanova, D.; Sebaai, F.; van Dorp, D. H.; Milenin, A.; Lin, D.; Nyns, L.; Mitard, J.; Pourghaderi, A.; Douhard, B.; Richard, O.; Bender, H.; Boccardi, G.; Caymax, M.; Heyns, M.; Vandervorst, W.; Barla, K.; Collaert, N.; Thean, A. V. Y. In *An InGaAs/InP quantum well finfet using the replacement fin process integrated in an RMG flow on 300mm Si substrates*, VLSI Technology (VLSI-Technology): Digest of Technical Papers, 2014 Symposium on, June 9−12, 2014, 2014; pp 1−2.
(21) Merckling, C.; Waldron, N.; Jiang, S.; Guo, W.; Barla, K.; Heyns, M.; Collaert, N.; Thean, A.; Vandervorst, W. *ECS Trans.* **2014**, *64* (6), 513−521.
(22) Nahory, R. E.; Pollack, M. A.; Johnston, W. D.; Barns, R. L. *Appl. Phys. Lett.* **1978**, *33* (7), 659−661.
(23) Coldren, L. A.; Corzine, S. W.; Mashanovitch, M. L. *Diode Lasers and Photonic Integrated Circuits*, 2nd ed.; John Wiley & Sons, Inc.: Hoboken, NJ, 1995.
(24) Koch, T. L.; Bowers, J. E. *Electron. Lett.* **1984**, *20* (25), 1038−1040.



DOI: 10.1021/acs.nanolett.6b04690
*Nano Lett.* 2017, 17, 559−564